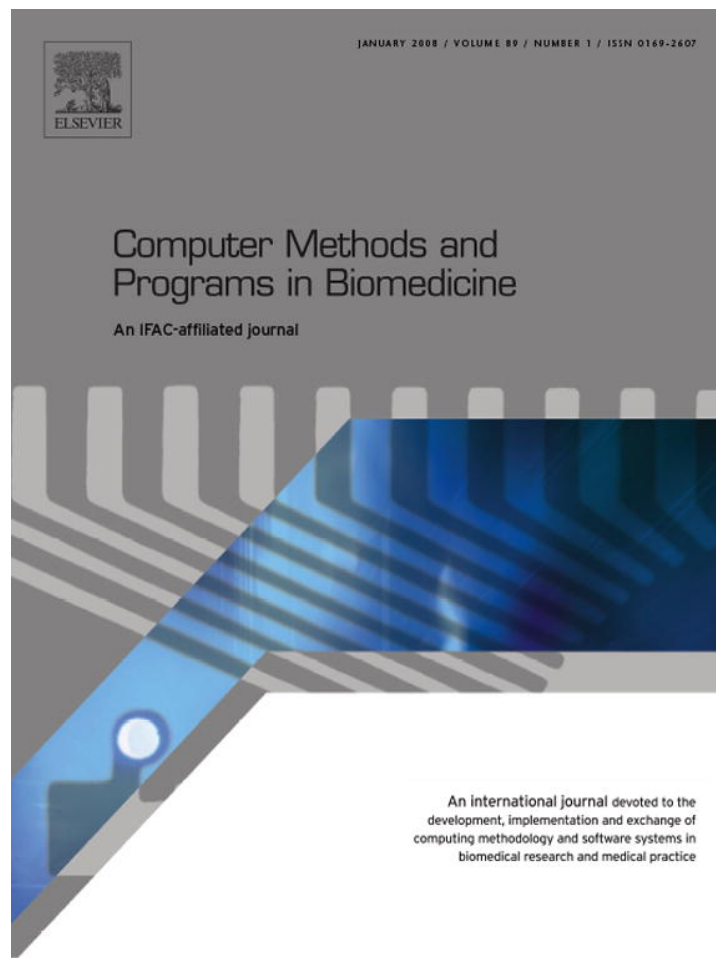


Provided for non-commercial research and education use.
Not for reproduction, distribution or commercial use.



This article was published in an Elsevier journal. The attached copy is furnished to the author for non-commercial research and education use, including for instruction at the author's institution, sharing with colleagues and providing to institution administration.

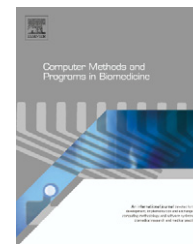
Other uses, including reproduction and distribution, or selling or licensing copies, or posting to personal, institutional or third party websites are prohibited.

In most cases authors are permitted to post their version of the article (e.g. in Word or Tex form) to their personal website or institutional repository. Authors requiring further information regarding Elsevier's archiving and manuscript policies are encouraged to visit:

<http://www.elsevier.com/copyright>



ELSEVIER

journal homepage: www.intl.elsevierhealth.com/journals/cmpb

Light transport in tissue by 3D Monte Carlo: Influence of boundary voxelization

T. Binzoni^{a,b,*}, T.S. Leung^c, R. Giust^d, D. Rüfenacht^b, A.H. Gandjbakhche^e

^a Centre Médical Universitaire, 1, r. Michel-Servet, Département des Neurosciences Fondamentales, University of Geneva, 1211 Genève 4, Switzerland

^b Département de l'Imagerie et des Sciences de l'Information Médicale, University Hospital, Geneva, Switzerland

^c Department of Medical Physics and Bioengineering, University College, London, UK

^d Département d'optique P.M. Duffieux, Institut FEMTO-ST, UMR CNRS 6174, Université de Franche Comté, Besançon, France

^e Laboratory of Integrative and Medical Biophysics, National Institute of Child Health and Human Development, National Institutes of Health, Bethesda, MD, USA

ARTICLE INFO

Article history:

Received 16 May 2007

Received in revised form

9 October 2007

Accepted 9 October 2007

Keywords:

Biomedical optics

Monte Carlo

Photon transport

Tissue phantom

Voxels

ABSTRACT

Monte Carlo (MC) based simulations of photon transport in living tissues have become the “gold standard” technique in biomedical optics. Three-dimensional (3D) voxel-based images are the natural way to represent human (and animal) tissues. It is generally believed that the combination of 3D images and MC based algorithms allows one to produce the most realistic models of photon propagation. In the present work, it is shown that this approach may lead to large errors in the MC data due to the “roughness” of the geometrical boundaries generated by the presence of the voxels. In particular, the computed intensity of the light detected on the tissue surface of a simple cubic tissue phantom may display errors from –80% to 120%. It is also shown that these errors depend in a complex manner on optical and geometrical parameters such as the interoptode distance, scattering coefficient, refractive index, etc. and on the degree of voxelization (“roughness”) of the boundaries. It is concluded that if one wants to perform reliable 3D Monte Carlo simulations on complex geometries, such as human brain, skin or trabecular bone, it is necessary to introduce boundary meshing techniques or other equivalent procedures in the MC code to eliminate the deleterious effect of voxelization.

© 2007 Elsevier Ireland Ltd. All rights reserved.

1. Introduction

Simulation techniques to describe light transport in tissues are considered to be fundamental tools in biomedical optics. Among the different approaches available, the Monte Carlo (MC) based methods represent a “gold standard”. MC based methods are utilised for wavelengths from the visible to the near infrared (NIR) range, covering in this way a large domain

of non-ionizing radiations and thus allowing the investigation of a large set of possible biomedical applications.

In the NIR domain, MC based methods have been successful because of their ability to test the validity of complex analytical algorithms obtained from the radiative transport equation. These analytical algorithms allow one to derive, from the experimental optical signals, quantities of fundamental medical interest such as tissue oxy- and deoxy-

* Corresponding author Tel.: +41 22 37 95 358; fax: +41 22 37 95 402.

E-mail address: Tiziano.Binzoni@medecine.unige.ch (T. Binzoni).

0169-2607/\$ – see front matter © 2007 Elsevier Ireland Ltd. All rights reserved.

doi:10.1016/j.cmpb.2007.10.008

haemoglobin concentrations, oxygen saturation [1], tissue blood speed/flow [2] etc. and for this reason testing procedures have great importance. It must be noted that it is also possible to use the MC approach to test image reconstruction methods used in NIR topography and tomography [3–7]. On the other hand, MC simulations permit one to directly “generate” new numerical algorithms allowing one to solve the so-called “inverse problem”. In fact, intuitively, the synthetic data derived from MC simulations can be utilised to directly “fit” real experimental optical data and thus obtain the wanted parameters [8–14]. This latter approach is particularly interesting when analytical solutions are too complex or even impossible to obtain. Other areas where MC methods have found value include calculating power deposits in laser treatment of port wine stains [15] modelling photoacoustic imaging [16], laser-doppler perfusion and tissue fluorescence [17].

Finally, besides the former straightforward applications of MC, there is also a need to better understand the relationship between measured optical parameters and the underlying tissue physiology. This can be done for example, by analysing the derived optical quantities against suitable theoretical models describing the physiology of the investigated tissue [18]. This approach was originally initiated by the international project known as the Physiome Project [19] and the biological mathematical models have already reached a high level of complexity, see Ref. [20]. For these models, hundreds of physiological parameters can be taken into account, the majority of which will probably not be (easily) measurable *in vivo*. By combining a MC based model, describing the transport of light in a tissue with complex structure, with a biological model [20] describing the physiology of the tissue, one can produce what we call here a Virtual Optical Human Phantom (VOHP). This includes also by definition the examples given in the previous paragraphs that may be seen as a virtual optical instrument allowing one to obtain optical data, generate or test algorithms or, “understand” the relationship existing between the underlying physiological variables and the experimental optical data through the physiological/biochemical aspects.

If these models are to generate reliable optical data, it is clear that the precision of the reproduction of the anatomical features (“geometry”) defining the VOHP becomes a key factor and as we will see in the present work, an approximated geometry might give significantly incorrect results and thus may not be regarded as a “gold standard”. In practice, the most common way to obtain larger scale anatomical information is to use standard medical images such as MRI, CT, PET, etc. For smaller features, as in the case of the description of human skin for studies of port-wine stains for NIR laser therapy, microscopic techniques such as optical coherence tomography (OCT) are of course more suitable. All of these techniques allow one to obtain personalised numerical 3D images related to a real and unique patient. A common feature of all these 3D images is that they are composed of a set of voxels which means that the boundaries of the anatomical structures (e.g. organs) are not smooth as they are in reality but are represented as irregular surfaces composed of the “corners” of the voxels and this might in principle influence the results of the MC simulations. It has already been shown that in the case of thin slabs representing the human skin, the presence of rough random surfaces at the interfaces (described by

a stationary random Gaussian process) can lead to significant differences in the estimation of the tissue optical parameters [21]. Similar problems have also been found with periodic roughness of a sinusoidal type [22]. Thus, there is good evidence to believe that voxelization of human anatomy might also introduce distortion in MC results. Such potential errors may be of considerable importance especially when exact or comparable values are needed. This is the case for example for the theoretical evaluation of the laser power needed for port-wine stains treatment [23,24]. Moreover, if the size of the errors varies for example with the spatial position of the light source/detectors, then it may become impossible to test/reproduce analytical models.

The problem of voxelization is usually neglected in biomedical optics or considered not important especially in the case where the different indexes of refraction of the tissues are set to the same value (i.e. no reflection/refraction is assumed or even made equal to the external medium) [15,23,25–27]. Moreover, even if the study of the Fresnel reflectance of rough boundaries is a fruitful domain of research [28], to our knowledge, there are no studies explicitly describing the voxelization problem. In practice, the size of the voxels is usually large compared to the utilized wavelength (especially in the NIR domain) and thus the boundaries appear practically smooth to the incident light from the local point of view and this is considered not to be an interesting problem because this can be described with the usual reflection/refraction laws.

The aim of the present work was to investigate the influence of voxelization on the optical quantities obtained by the MC simulations and thus on the applications cited above. To be more precise this work does not seek to discuss the influence of the roughness of the surface of a “real” tissue/organ, but to consider the roughness generated by the 3D imaging systems with a finite precision and represent images as 3D voxels.

For simplicity, because of the almost infinite number of possible simulations, in this paper we only consider the case of CW radiation and a very simple geometrical form, where for comparison an exact solution can also be obtained (i.e. without the influence of the voxelization). This has the advantage of clearly identifying the different effects of the voxelization.

2. Material and methods

2.1. Computer cluster

The VOHP was built on a cluster of nine computers (DELL™, OptiPlex GX620, USA) having CPUs running at 3.2 GHz. In fact, MC simulations of light transport are ideal to be implemented as distributed calculations [29]. One computer was utilized as a client, distributing the jobs to the remaining eight. The MC code was developed in MATLAB® 7.2 language (The Mathworks, Inc, Natick, MA, USA) and the interaction between the computers was controlled by the MATLAB® Distributed Computing Engine 2. This schedules and evaluates tasks on multiple remote MATLAB® sessions, reducing execution time compared to running in a single MATLAB® session. This approach allows a very fast prototyping of the MC code by taking advantage of the already built-in mathematical and

graphical functions in Matlab. It has been estimated that a gain of a time factor of ~ 7.5 can be obtained with eight machines compared to only one.

2.2. The 3D Monte Carlo code

The MC code is based on the theory already tested by Pfeifer et al. [25] but the present code can be distributed on an inhomogeneous or homogeneous cluster. The main point is that the tissue geometry is represented by a 3D matrix of voxels (i.e. rectangular parallelepipeds), all of the same size, which can be obtained from any of the conventional medical imaging modalities. The 3D matrix elements can have only positive integer values and an integer corresponds to a given tissue (e.g. brain, muscle, etc., defining the corresponding voxel). Air is usually set to zero. The voxel size is stored in a separated variable. The optical parameters, related to a voxel, such as the absorption coefficient ($\mu_a \text{ mm}^{-1}$), scattering coefficient ($\mu_s \text{ mm}^{-1}$), phase function, etc. are stored in a structure labelled by the corresponding integer number. The only condition is that the two outermost layers of voxels (i.e. at the boundaries of the cube defined by the 3D matrix) must represent the air (i.e. voxel value set to zero). In practice, this means that the studied geometry is always completely contained in the region defined by the 3D matrix and that the photons are terminated if they reach the voxels composing

these layers (they reach the air). The remaining voxels can represent indiscriminately any tissue or air.

It is important to notice that when the geometry represents, for example, a set of slabs with their faces parallel to the x - y axis (and the only utilised phase function is the Henyey–Greenstein function) then the MC code is equivalent to the well-known classical MC code proposed by Prahl et al. [30] and Wang et al. [31].

2.3. Chosen geometry for the VOHP

To show the influence of the boundary voxelization and to quantify the potential errors induced in the data generated by the MC simulations we have chosen a very simple and didactical case. The basic phantom was represented by a $256 \times 256 \times 256$ matrix (i.e. the equivalent number of voxels) corresponding to a cubic region of 250 mm edge, inside which the simulated “tissue” was situated. At the center of this region there was a cube, representing a homogeneous tissue, composed of $132 \times 132 \times 132$ voxels (the remaining voxels outside this region represented the air). Thus, in this simple case, the VOHP is composed of the tissue plus the air around it. The tissue edge in this case measures ~ 128.9 mm and one voxel edge ~ 0.98 mm.

The CW light source was an infinitely narrow beam of photons situated at the center and normal to one of the faces of the

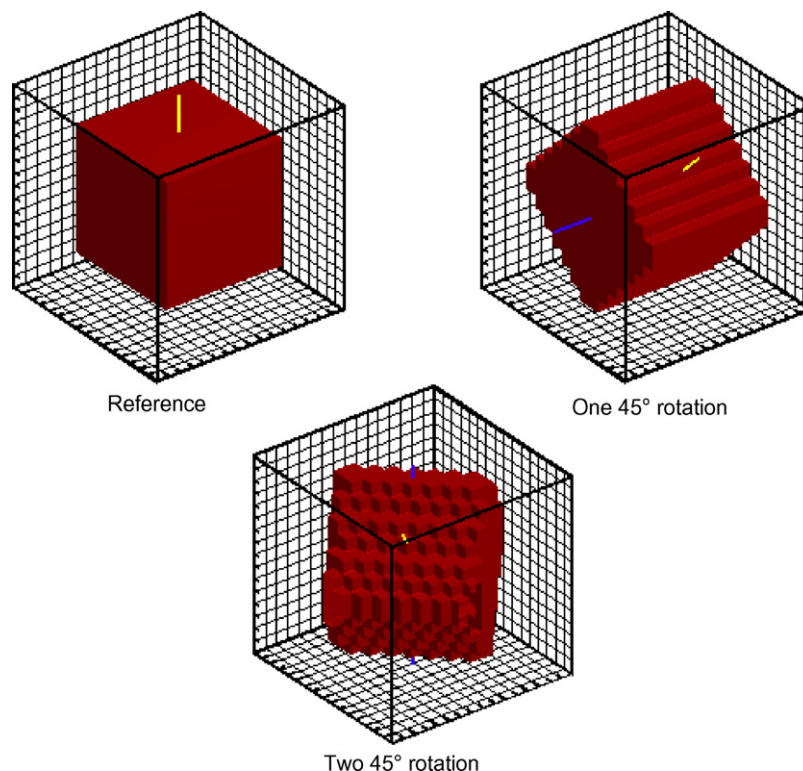


Fig. 1 – The cubic region defined by the black lines represents the phantom ($16 \times 16 \times 16$ matrix to facilitate the visualization of the voxels that obviously would not be visible with a $256 \times 256 \times 256$ matrix) and the grids represent the projection of the voxels on the cartesian x - y - z planes. The brown cube represents the tissue and the “invisible” remaining volume around the tissue corresponds to the air. The tissue cube is represented in three different positions i.e., with the faces parallel to the x - y - z planes (reference); after a 45° rotation around the y axis; and after a further rotation around the z axis. The blue line represents the rotation axis. The yellow line represents the light source (e.g. optical fibre normal to the tissue face). (For interpretation of the references to color in this figure legend, the reader is referred to the web version of the article.)

tissue cube (along the z axis). The detector was also placed normal to the same face at a distance r (mm) from the source (the interoptode distance). The intensity of the photons detected at a distance r from the source, $R(r)$, was expressed as a photon probability per unit area (mm^{-2}) and this was the simulated parameter.

The large size of the cube, allowed us to consider the “tissue” as a semi-infinite medium. This assumption was tested by comparing the present model with a classical simulation describing a real semi-infinite medium (the results are not shown here since this does not directly concern the aim of the study). In this case, the problem can be considered as having a cylindrical symmetry and this property has been exploited as usual to improve the signal to noise ratio [30,31]. A simplified version, i.e. for a $16 \times 16 \times 16$ matrix, of this phantom can be seen in Fig. 1.

To estimate the influence of voxelization on the MC simulated $R(r)$, the cubic tissue was placed in three different positions compared to the planes defined by the x - y - z axes (see Fig. 1). The reference simulations were performed with the cube faces parallel to the axes planes. It is obvious that in this case one finds the exact values for $R(r)$ because the faces are actually “flat”. The other simulations were then run with the tissue cube rotated 45° around the y axis and repeated again after a further rotation of 45° around the z axis. In the latter two cases, due to the fact that the phantom is built with voxels, the faces cannot remain flat after the rotations and this effect is clearly seen also in Fig. 1. To make this effect visible to the eye, in Fig. 1 we have utilized only a $16 \times 16 \times 16$ matrix. In the case where the phantom is a $256 \times 256 \times 256$ matrix (as for all the performed simulations), this “roughness” is impossible to be seen because it is too tiny. This might be one of the reasons why this “roughness” is usually considered as negligible in simulations.

Based on the above definitions, the aim of the present work was to investigate the potential errors induced on the $R(r)$ estimation by the boundary voxelization. The percentage error was computed by comparing the $R(r)$ values obtained before rotation (reference) with those obtained after y and y - z rotation. Theoretically we would like to have exactly the same results for the three cases, because the geometry (source and detector included) is just rotated but not changed (i.e. the physics should remain strictly the same).

2.4. Details of the MC model

To improve the signal to noise and the efficiency of the simulations, the implicit photon capture variance reduction technique was utilised [32]. The photon packet propagation was terminated when it reached the air (i.e. at the detection site) or by the roulette termination technique [32]. The trigger value engaging the roulette algorithm was fixed at $W < 1 \times 10^{-4}$ and the photon packet had a chance of 1/10 to survive with a new weight, $10W$.

The photon packet steps were generated by means of the variable step size method [30]. This means that the probability density for a photon to make a step of size $s \in [0, +\infty)$ was given by:

$$p_s(s) = (\mu_a + \mu_s)e^{-(\mu_a + \mu_s)s} \quad (1)$$

If s is sampled in this manner, it is equivalent to saying that the photon is forced to be absorbed or scattered after each step (there is no possibility for no interaction, as could be the case if s is very small).

The model describing the change in direction of a photon packet after a collision, in a biological tissue, was represented by the Henyey–Greentein scattering phase function [33]. In practice, in the MC simulation, this model was expressed in probabilistic terms by means of two probability density functions:

$$p_\theta(\theta) = \frac{1}{2} \frac{(1 - g^2) \sin(\theta)}{(1 + g^2 - 2g \cos(\theta))^{3/2}} \quad (2)$$

and

$$p_\phi(\phi) = \frac{1}{2\pi} \quad (3)$$

where $\theta \in [0, \pi]$, $\phi \in [0, 2\pi)$ and $g \in [-1, 1]$ are the deflection and azimuthal angle of the direction change and the anisotropic factor, respectively.

Reflection at boundaries was taken into account using the Snell–Descartes' and Fresnel's formulas. For the sake of completeness, the air-tissue index mismatch was also taken into account when injecting the photons in the tissue however, this was not an essential point for the present purposes. Reflection on all boundaries was treated as an all-or-none problem, i.e. the photon packet is either completely reflected or completely transmitted based on a probability derived from Fresnel's law. This simplifies the problem of managing multiple simultaneous reflections of split photon packets found in the partial reflection approach.

The core of a MC simulation is represented by the pseudo-random number generator allowing to obtain the distributions for $p_s(s)$, $p_\theta(\theta)$, $p_\phi(\phi)$, etc or allowing to make a probabilistic choice such as the probability thresholds defined by $P_{\text{reflection}}(\alpha_i)$ (Fresnel law) or the roulette algorithm (i.e. the 1×10^{-4} value). The distributions were obtained by the method proposed by [34], implemented in this work by using a modified version of the Marsaglia's “subtract with borrow” algorithm [35] already implemented in the MATLAB® language. The algorithm can theoretically generate over 2^{1492} values before repeating itself. During the distributed computations the pseudo-random number generator of each computer was randomly and independently initialised to ensure the generation of different random numbers in each computer.

In practice, the MC code utilized in the present work reproduces exactly the same “physics” as the classical MC code proposed by Prah et al. [30] and Wang et al. [31] but with a fundamental difference that it allows to simulate more complex geometries (the voxelization problem in our case). This advantage has the drawback to considerably increase the computation time (tests and computations must be performed each time a photon packet goes from one voxel to the next one) and this is why it is better to run the code on a computer cluster configuration.

2.5. Source and detection points position

As explained in Section 2.3 the source is placed at the center of one of the surfaces of the tissue reference cube. Given

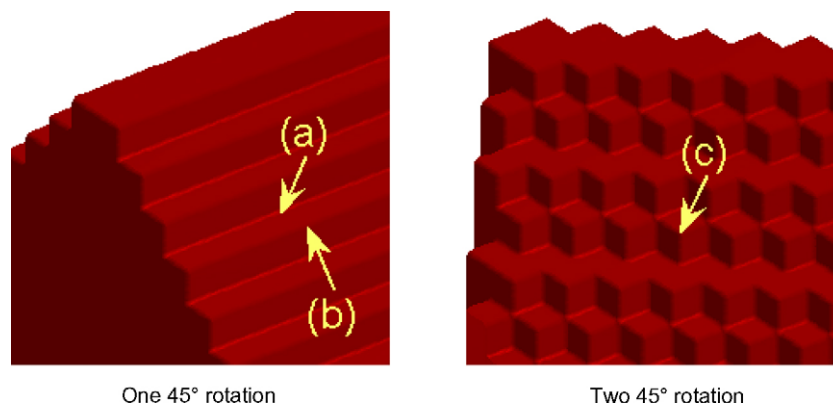


Fig. 2 – Possible source positions (yellow arrows) utilized for the simulations (see text). The photons are always considered to be injected “normal” to the tissue surface. (For interpretation of the references to color in this figure legend, the reader is referred to the web version of the article.)

the large size of the reference phantom it is clear that even if one shifts the source (on the surface) by a length of the order of one pixel, the MC simulations will produce strictly the same $R(r)$. This should be true even for the phantoms represented by the rotated reference (Fig. 1). In reality, after rotation of the phantom, the tissue surface is no longer flat, due to the presence of the voxels, and in this case we are obliged to choose where we want to place the source (e.g. on a voxel “corner” or on an “edge” defined by two voxels, etc.). This problem is usually neglected, because one considers that the voxels are so small that they have no influence in this regard. It must be noted that in practice, a similar hypothesis is always made when placing the source on a tissue surface defined for example on a 3D human head obtained by MRI. In the present paper we will show that this problem cannot be neglected and that the source position has an influence on the MC simulated data. Thus, for explanatory reasons we have chosen the set of configurations appearing in Fig. 2 for the source positions in the different simulations.

2.6. Parameters and calculations common to all the simulations

Each MC simulation was repeated for each of the three VOHP configurations appearing in Fig. 1. This gave three sets of results to be compared per type of simulation. The error in the computed $R(r)$ after one or two 45° rotations was defined as the percentage difference from the exact solution obtained with the reference VOHP configuration.

The fixed optical parameters for the air were: $\mu_a = 0 \text{ mm}^{-1}$, $\mu_s = 0 \text{ mm}^{-1}$; and for the tissue: $\mu_a = 0.025 \text{ mm}^{-1}$. Each MC simulation (and configuration) was also methodically repeated for a tissue reduced scattering coefficients $\mu'_s = \mu_s(1 - g)$ equal to 0.15, 0.6 and 2.0 mm^{-1} .

The number of photon packets for one MC simulation run was 2,880,000 when μ'_s was equal to 0.15 or 0.6 mm^{-1} , and 4,320,000 when μ'_s was equal to 2.0 mm^{-1} . To estimate the standard deviation of the computed $R(r)$, the simulations obtained with μ'_s equal to 0.15 or 0.6 mm^{-1} were split into six

sub-simulations, and with μ'_s equal to 2.0 mm^{-1} were split into nine sub-simulations [32]. This gave 480,000 photon packets per sub-simulation. In this way, by using the sub-simulations, it has been possible to estimate the means and the standard deviations of the different quantities appearing in the figures [32]. The source-detector distance was chosen in the interval $r \in [0,40]$ mm when μ'_s was equal to 0.15 or 0.6 mm^{-1} and $r \in [0,32]$ when μ'_s was equal to 2.0 mm^{-1} .

2.7. Simulation 1

In this simulation we set $n=1.4$ and $g=0$. This choice of parameters reproduces the classical diffusion approximation problem and in the literature it has been usually utilised to test a great number of equivalent analytical models derived from the radiative transport theory. For the first 45° rotation configuration, the source was set at position (b) (see Fig. 2) and for the second 45° rotation configuration at position (c).

2.8. Simulation 2

In this simulation one has utilised $n=1$ and $g=0$. This choice of parameters also reproduces the classical diffusion approximation problem. However, in this case there is no difference between the refractive index of air and the tissue (no index mismatch). This means that in practice the photons are not reflected on the boundaries and thus the voxelization should not have a large influence on the precision of the MC results. For the first 45° rotation configuration, the source was set at position (b) (see Fig. 2) and for the second 45° rotation configuration at position (c).

2.9. Simulation 3

The simulation parameters were the same as in simulation 1, however, in this case the source was set at position (a) (see Fig. 2). The aim was to investigate if the source position (a shift of only one voxel) really has no influence on the MC results as it is often assumed in the literature when working for example at large interoptodes distance (i.e. at a many voxel size distance).

2.10. Simulation 4

In this simulation we set $n=1.4$ and $g=0.9$. This parameters choice should reproduce a “real” situation where the tissue is not isotropic and where there is an index mismatch between the air and the medium. In this case the diffusion approximation (especially at short interoptode distance) does not hold. If one wants to describe these MC data with an analytical solution it is necessary to use a more complex approximation of the radiative transfer equation than the diffusion regime. For the first 45° rotation configuration, the source was set at position (b) (see Fig. 2) and for the second 45° rotation configuration at position (c).

2.11. Simulation 5

This simulation is a simple case study allowing to investigate the influence of different μ_a values on $R(r)$. For this reason μ'_s was set to 0.6 mm^{-1} and μ_a values were chosen equal to 0.005 , 0.5 and 0.1 mm^{-1} . The remaining parameters were set at $n=1.4$ and $g=0$. For the first 45° rotation configuration, the source was set at position (b) (see Fig. 2) and for the second 45° rotation configuration at position (c).

3. Results

In all the figures showing the results (Figs. 3–6) we have used the same abscissa and ordinate scale limits to facilitate data comparison. The ordinate axis of these figures represents the error on $R(r)$ expressed as a percentage of the exact values computed using the reference phantom. The abscissa axis represents the interoptode distance r . The only exception is Fig. 5

where the right panel reports the “relative” error on $R(r)$ (see below). The three lines appearing in each figure are always derived from the MC simulations using μ'_s equal to 0.15 , 0.6 and 2.0 mm^{-1} , and appear as a red, black and blue line. In this case, if the reduced total attenuation coefficient is expressed as $\mu'_t = \mu_a + \mu'_s$, then the transport corrected mean free path for an attenuation event, $1/\mu'_t$, were ~ 5.72 , ~ 1.6 and $\sim 0.49\text{ mm}$, respectively. Thus, if $\mu'_s = 0.15\text{ mm}^{-1}$, then the mean photon (packet) steps were larger than the voxel size ($\sim 0.98\text{ mm}$) and for $\mu'_s = 2.0\text{ mm}^{-1}$, they were smaller. As already noted in the Methods section, the data for $\mu'_s = 2.0$ are always reported only for $0 < r < 32$ because the standard deviation of the error becomes too large for $r \geq 32$. It would require an enormous amount of additional computer time to further reduce the standard deviation. It should be noted that the particular parameters values $\mu_a = 0.025\text{ mm}^{-1}$ and $\mu'_s = 0.6\text{ mm}^{-1}$ are typical of human skeletal muscle.

3.1. Simulation 1

This MC simulation represents a typical “diffusive” transport of the photon packets. From Fig. 3 it clearly appears that the structure of the surface (due to the presence of the voxels) influences the magnitude of the errors on $R(r)$. In practice, for a given interoptode distance, the more “rough” the simulated surface is, e.g. after two 45° rotations compared to only one, the larger is the error of the computed $R(r)$. The error magnitude globally decreases with increasing r . The largest errors are found for small ($r < 5\text{ mm}$) interoptode distance, independent of the chosen μ'_s values. These observations seem to be generally applicable, i.e. they are observed in all the simulations (see also below), if the source is set on a voxel “edge” (Fig. 2, positions (b) and (c)).

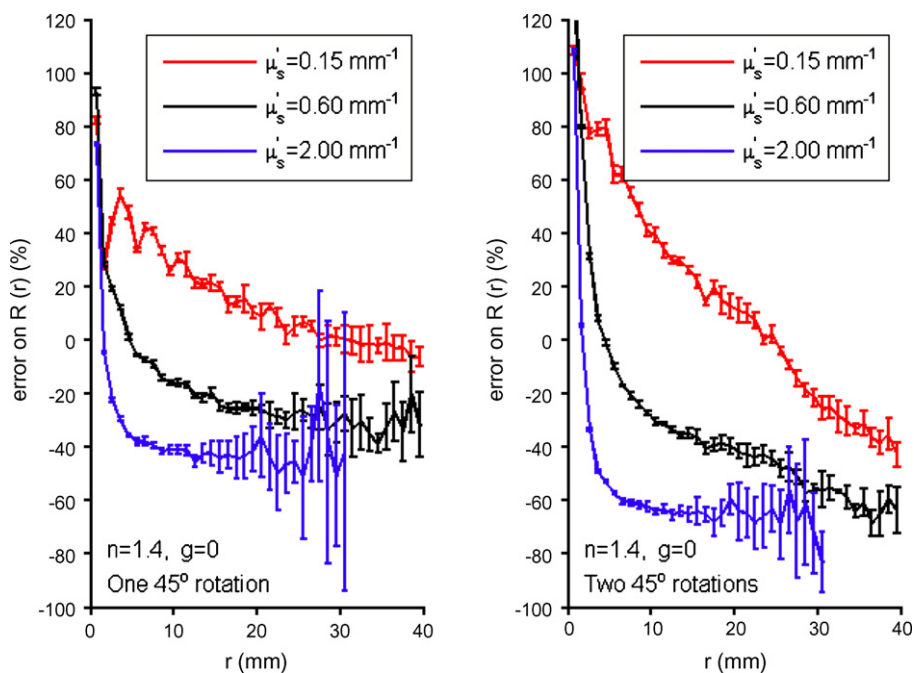


Fig. 3 – Percentage error on $R(r)$ as a function of r after one 45° rotation and two 45° rotations. The error is computed by comparison with the exact solution for $R(r)$ obtained with the reference phantom (see Fig. 1). The source position is (b) (see Fig. 2). The vertical bars are standard deviations.

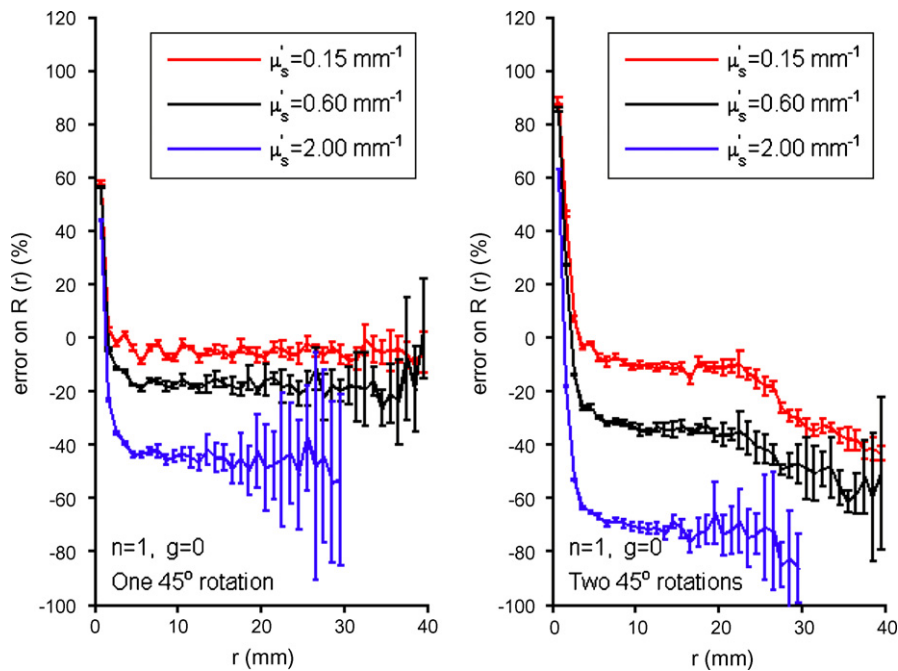


Fig. 4 – Percentage error on $R(r)$ as a function of r after one 45° rotation and two 45° rotations. The error is computed by comparison with the exact solution for $R(r)$ obtained with the reference phantom (see Fig. 1). The source position is (b) (see Fig. 2). The vertical bars are standard deviations.

3.2. Simulation 2

This simulation shows that even if the refractive indices are matched (air/tissue), the errors on $R(r)$ do not disappear

(Fig. 4). Globally the results can be described as in simulation 1 although the errors appear to be smaller. The better results for $R(r)$ (i.e. when the error is near zero) seem to be obtained when the mean photon (packet) step is a lot larger

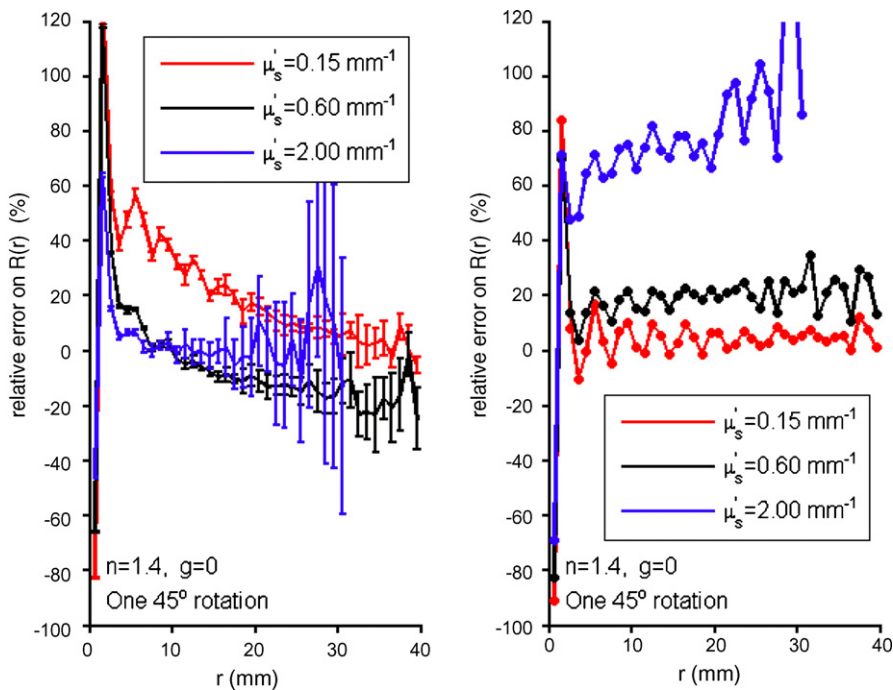


Fig. 5 – Left) Percentage error on $R(r)$ as a function of r after one 45° rotation. The error is computed by comparison with the exact solution for $R(r)$ obtained with the reference phantom (see Fig. 1). The source position is (a) (see Fig. 2). Right) Relative error on $R(r)$ as a function of r after one 45° rotation. The relative error is computed by comparing the $R(r)$ values obtained for a source position (b) and (a) (see Fig. 2). The vertical bars are standard deviations.

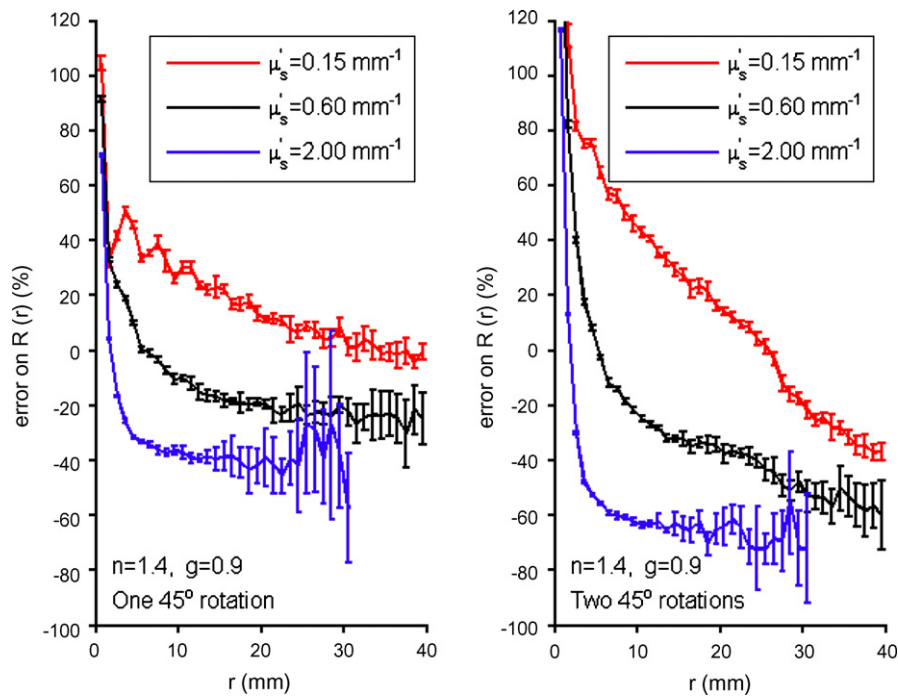


Fig. 6 – Percentage error on $R(r)$ as a function of r after one 45° rotation and two 45° rotations. The error is computed by comparison with the exact solution for $R(r)$ obtained with the reference phantom (see Fig. 1). The source position is (b) (see Fig. 2). The vertical bars are standard deviations.

than the voxel size (i.e. when $\mu'_s = 0.15$), however, this is not a general rule valid for the other simulations. Unfortunately, the errors remains very large, even for $\mu'_s = 0.15$, when $r < 5$ mm.

3.3. Simulation 3

The results reported in Fig. 5 (left) show that there is an extreme sensitivity to the source position (see Fig. 2). In fact,

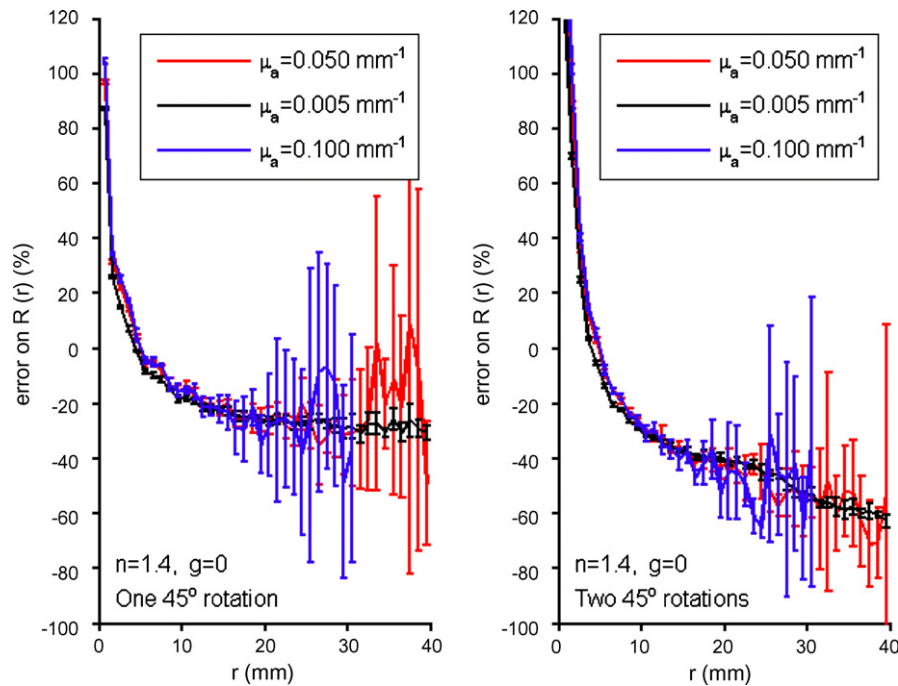


Fig. 7 – Percent error on $R(r)$ as a function of r after one 45° rotation and two 45° rotations. The error is computed by comparison with the exact solution for $R(r)$ obtained with the reference phantom (see Fig. 1). The source position is (b) (see Fig. 2). The vertical bars are standard deviations. In this special case μ'_s was fixed to 0.6 mm^{-1} for all the curves appearing in the figure.

if one compares Figs. 3 and 5 (the single 45° rotation case) one can see that the error on $R(r)$ varies in an unpredictable manner depending on the source position (position (b) for Fig. 3 and (a) for Fig. 5). To estimate the magnitude of the difference generated by position (b) and (a), the relative change in error (in percent) of (a) compared to (b) is reported in Fig. 5 (right). One can see that there is no ideal source position allowing one to obtain exact $R(r)$ values (intermediate source positions on the voxel will give intermediate values between Figs. 3 and 5 but not nil errors).

3.4. Simulation 4

This simulation (Fig. 6) is aimed to simulate an ideal “real” condition, where the photon packets propagate in an anisotropic medium. Even in this case the error on $R(r)$ is not negligible and it depends in a complex manner on r , μ'_s and on the degree of voxelization of the boundaries.

3.5. Simulation 5

The results of this simulation are reported in Fig. 7. From this figure it can be seen that μ_a curves are very similar, showing that the error on $R(r)$ is independent of the values of μ_a . It is likely that the errors seen here are mainly due to the value of μ'_s , obtained using different μ_a . However, we must not neglect the fact, that for small r values (e.g. $r < 5$ mm) the error on $R(r)$, for different μ_a , may differ more than 20% and thus that for small r the effect of μ_a is not completely negligible even if μ'_s still remain the main source of error.

4. Discussion and conclusions

In the introduction section the importance of being able to deduce exact $R(r)$ values from MC simulations, and especially in the case of complex tissue geometries, was explained and the point was made that 3D voxel-based images are the most natural way to represent tissues.

The results of the simulations in this work demonstrate that this simple approach produces large errors, and the presence of the boundary voxelization may prevent their use as a “gold standard” for the testing of analytically derived algorithms. These errors depends in a complex manner on the optical and geometrical parameters such as r , μ'_s , n and on the degree of voxelization of the boundaries. It should be noted that this is true even in the simplest case where the light transport is considered diffusive and where the refractive indices are matched. The parameter μ_a also have an effect on the error on $R(r)$ however, its contribution seems to be a lot less pronounced in comparison to μ'_s (this needs to be further investigated). It is common practice to express $R(r)$ on a logarithmic scale because in the diffusion regime it decreases exponentially for increasing r . Voxelization maintains this same global decreasing trend, and this might allow one in the future to develop some correction algorithms eliminating this additional source of “noise” generated by the presence of the voxels.

The standard deviation of the MC results is presented here (Figs. 3–7). This allows the readers to assess for themselves

the quality of the MC simulations. It can be seen from these figures that the standard deviations of the MC results for certain parameters (e.g. $\mu'_s = 2.0 \text{ mm}^{-1}$) are large for $r > \sim 15$ mm, suggesting more simulations should be carried out. However, the general trends on the error on $R(r)$ can still be identified from the mean values for $r > \sim 15$ mm.

The voxelization problem must be studied on a case by case basis depending on the parameters used. The above comments are of course only true if one has the presence of boundary voxelization. However, if all the boundaries (for any complex geometry with many tissues) are parallel to one of the x - y - z planes, then the results for $R(r)$ obtained from MC simulations are obviously exact (i.e. our reference geometry).

By comparing Figs. 3, 4 and 6, it is noted that the refractive index appears to have a greater influence on the computed error on $R(r)$ than g . Thus, results have to be carefully interpreted when both voxelization and refractive index mismatch occur at the same time.

The simulations performed in the present work were performed for a point like source. It would be interesting to know the results for a more general light beam source with a finite aperture. Unfortunately, the convolution technique usually utilized to derive the $R(r)$ values for a finite beam source cannot be applied with the presence of voxelization. However, one would expect that the errors on $R(r)$ would still remain even for a finite beam source. To properly assess the effects of a finite beam source, the MC simulations can be performed with point sources over a finite area. To simplify the problem, we only consider a point source in this paper. Further investigations on this subject are obviously necessary.

We conclude that, in general, if one wants to perform reliable 3D MC simulations of complex tissue geometries such as human brain, skin or trabecular bone, it is probably necessary to introduce boundary meshing techniques [36] or other equivalent procedure in the MC code to eliminate the deleterious effect of boundary voxelization. This means that in this case the boundaries will be “smoother” or “blunter” surface angles and thus theoretically decreasing the errors. These considerations must not be neglected for a large range of wavelengths going from visible to NIR radiation.

Acknowledgments

We thank the “Faculté de Médecine” of Geneva for the Mimosa grant that has allowed the setting up of the computer cluster. A.G. acknowledge the support of this research by the Intramural Research Programs of the National Institute of Child Health and Human Development, NIH.

REFERENCES

- [1] M. Ferrari, L. Mottola, V. Quaresima, Principles, techniques, and limitations of near infrared spectroscopy, *Can. J. Appl. Physiol.* 29 (4) (2004) 463–487.
- [2] J.D. Briers, Laser Doppler, speckle and related techniques for blood perfusion mapping and imaging, *Physiol. Meas.* 22 (4) (2001) R35–R66.

- [3] S.R. Arridge, M. Cope, D.T. Delpy, The theoretical basis for the determination of optical pathlengths in tissue: temporal and frequency analysis, *Phys. Med. Biol.* 37 (7) (1992) 1531–1560.
- [4] S.R. Arridge, J.C. Hebden, Optical imaging in medicine: II. modelling and reconstruction, *Phys. Med. Biol.* 42 (5) (1997) 841–853.
- [5] L. Dagdug, G.H. Weiss, A.H. Gandjbakhche, Effects of anisotropic optical properties on photon migration in structured tissues, *Phys. Med. Biol.* 48 (10) (2003) 1361–1370.
- [6] A.P. Gibson, J.C. Hebden, S.R. Arridge, Recent advances in diffuse optical imaging, *Phys. Med. Biol.* 50 (4) (2005) R1–R43.
- [7] T. Yates, J.C. Hebden, A. Gibson, N. Everdell, S.R. Arridge, M. Douek, Optical tomography of the breast using a multi-channel time-resolved imager, *Phys. Med. Biol.* 50 (11) (2005) 2503–2517.
- [8] V.G. Peters, D.R. Wyman, M.S. Patterson, G.L. Frank, Optical properties of normal and diseased human breast tissues in the visible and near infrared, *Phys. Med. Biol.* 35 (9) (1990) 1317–1334.
- [9] J.F. Beek, H.J. van Staveren, P. Posthumus, H.J. Sterenborg, M.J. van Gemert, The optical properties of lung as a function of respiration, *Phys. Med. Biol.* 42 (11) (1997) 2263–2272.
- [10] A. Pifferi, P. Taroni, G. Valentini, S. Andersson-Engels, Real-time method for fitting time-resolved reflectance and transmittance measurements with a Monte Carlo model, *Appl. Opt.* 37 (13) (1998) 2774–2780.
- [11] C.R. Simpson, M. Kohl, M. Essenpreis, M. Cope, Near-infrared optical properties of ex vivo human skin and subcutaneous tissues measured using the Monte Carlo inversion technique, *Phys. Med. Biol.* 43 (9) (1998) 2465–2478.
- [12] Y. Du, X.H. Hu, M. Cariveau, X. Ma, G.W. Kalmus, J.Q. Lu, Optical properties of porcine skin dermis between 900 nm and 1500 nm, *Phys. Med. Biol.* 46 (1) (2001) 167–181.
- [13] C.K. Hayakawa, J. Spanier, F. Bevilacqua, A.K. Dunn, J.S. You, B.J. Tromberg, V. Venugopalan, Perturbation Monte Carlo method to solve inverse photon migration problems in heterogeneous tissues, *Opt. Lett.* 26 (17) (2001) 1335–1337.
- [14] G.M. Palmer, N. Ramanujam, Monte Carlo-based inverse model for calculating tissue optical properties. Part I: Theory and validation on synthetic phantoms, *Appl. Opt.* 45 (5) (2006) 1062–1071.
- [15] T.J. Pfefer, J.K. Barton, D.J. Smithies, T.E. Milner, J.S. Nelson, M.J. van Gemert, A.J. Welch, Modeling laser treatment of port wine stains with a computer-reconstructed biopsy, *Lasers. Surg. Med.* 24 (2) (1999) 151–166.
- [16] B.T. Cox, S.R. Arridge, K.P. Kostli, P.C. Beard, Two-dimensional quantitative photoacoustic image reconstruction of absorption distributions in scattering media by use of a simple iterative method, *Appl. Opt.* 45 (8) (2006) 1866–1875.
- [17] A. Liebert, H. Wabnitz, H. Obrig, R. Erdmann, M. Moller, R. Macdonald, H. Rinneberg, A. Villringer, J. Steinbrink, Non-invasive detection of fluorescence from exogenous chromophores in the adult human brain, *Neuroimage* 31 (2) (2006) 600–608.
- [18] T. Binzoni, W. Colier, E. Hiltbrand, L. Hoofd, P. Cerretelli, Muscle O₂ consumption by NIRS: a theoretical model, *J. Appl. Physiol.* 87 (2) (1999) 683–688.
- [19] J.B. Bassingthwaite, Strategies for the physiome project, *Ann. Biomed. Eng.* 28 (8) (2000) 1043–1058.
- [20] M. Banaji, I. Tachtsidis, D. Delpy, S. Baigent, A physiological model of cerebral blood flow control, *Math. Biosci.* 194 (2) (2005) 125–173.
- [21] X. Ma, J.Q. Lu, X.H. Hu, Effect of surface roughness on determination of bulk tissue optical parameters, *Opt. Lett.* 28 (22) (2003) 2204–2206.
- [22] I.V. Meglinski, S.J. Matcher, Modelling the sampling volume for skin blood oxygenation measurements, *Med. Biol. Eng. Comput.* 39 (1) (2001) 44–50.
- [23] J.K. Barton, T.J. Pfefer, A.J. Welch, D.J. Smithies, J.S. Nelson, M.J.C. van Gemert, Optical Monte Carlo modelling of a true port wine stain anatomy, *Opt. Express* 2 (9) (1998) 391–396.
- [24] R. Zhang, W. Verkruyse, G. Aguilar, J.S. Nelson, Comparison of diffusion approximation and Monte Carlo based finite element models for simulating thermal responses to laser irradiation in discrete vessels, *Phys. Med. Biol.* 50 (17) (2005) 4075–4086.
- [25] T.J. Pfefer, J.K. Barton, E.K. Chan, M.G. Ducros, B.S. Sorg, T.E. Milner, J.S. Nelson, A.J. Welch, A three-dimensional modular adaptable grid numerical model for light propagation during laser irradiation of skin tissue, *IEEE J. Sel. Top. Quant. Electron.* 2 (4) (1996) 934–942.
- [26] D.A. Boas, J.P. Culver, J.J. Stott, A.K. Dunn, Three dimensional Monte Carlo code for photon migration through complex heterogeneous media including the adult human head, *Opt. Express* 10 (3) (2002) 159–170.
- [27] A. Custo, W.M. Wells III, A.H. Barnett, E.M. Hillman, D.A. Boas, Effective scattering coefficient of the cerebral spinal fluid in adult head models for diffuse optical imaging, *Appl. Opt.* 45 (19) (2006) 4747–4755.
- [28] I. Ohlidal, K. Navratil, M. Ohlidal, in: E. Wolf (Ed.), *Scattering of Light from Multilayer Systems with Rough Boundaries*, in *Progress in Optics XXXIV*, Elsevier Science, Amsterdam, 1995, pp. 249–331.
- [29] D.R. Kirkby, D.T. Delpy, Parallel operation of Monte Carlo simulations on a diverse network of computers, *Phys. Med. Biol.* 42 (6) (1997) 1203–1208.
- [30] S.A. Prahl, M. Keijzer, S.L. Jacques, A.J. Welch, A Monte Carlo code of light propagation in tissue, *Proc SPIE IS* 5 (1989) 102–111.
- [31] L. Wang, S.L. Jacques, L. Zheng, MCML—Monte Carlo modelling of light transport in multi-layered tissues, *Comput. Method. Program. Biomed.* 47 (2) (1995) 131–146.
- [32] I.M. Sobol, *The Monte Carlo Method*, Mir Publishers, Moscow, 1975.
- [33] L.G. Henyey, J.L. Greenstein, Diffuse radiation in the galaxy, *Astrophys. J.* 93 (1941) 70–83.
- [34] A.N. Witt, Multiple scattering in reflection nebulae: I. A Monte Carlo approach, *Astrophys. J.* 35 (1977) S1–S6.
- [35] C.B. Marsaglia, A. Zaman, A new class of random number generators, *Ann Appl Prob.* 3 (1991) 462–480.
- [36] K.H. Muci-Kuchler, J.C. Miranda, J.C. Miranda-Valenzuela, *Adaptive Meshing with Boundary Elements (Topics in Engineering)*, WIT Press, Wessex, 2002.